

Complex and variable crustal and uppermost mantle seismic anisotropy in the western United States

Fan-Chi Lin^{1*}, Michael H. Ritzwoller¹, Yingjie Yang¹, Morgan P. Moschetti¹ and Matthew J. Fouch²

The orientation and depth of deformation in the Earth is characterized by seismic anisotropy¹—variations in the speed of passing waves caused by the alignment of minerals under strain into a preferred orientation. Seismic anisotropy in the western US has been well studied^{2–11} and anisotropy in the asthenosphere is thought to be controlled by plate motions and subduction^{6–9}. However, anisotropy within the crust and upper mantle and the variation of anisotropy with depth are poorly constrained. Here, we present a three-dimensional model of crustal and upper mantle anisotropy based on new observations of ambient noise¹² and earthquake¹³ data that reconciles surface wave and body wave⁹ data sets. We confirm that anisotropy in the asthenosphere reflects a mantle flow field controlled by a combination of North American plate motion and the subduction of the Juan de Fuca and Farallon slab systems^{6–9}. We also find that seismic anisotropy in the upper mantle and crust are largely uncorrelated: patterns of anisotropy in the crust correlate with geological provinces, whereas anisotropy in the upper mantle is controlled by temperature variations. We conclude that any coupling between anisotropy in the crust and mantle must be extremely complex and variable.

Recent advances in surface wave methodology, particularly the development of ambient noise interferometry^{14,15}, improvements in ambient noise and earthquake tomography^{13,16,17}, and the ongoing deployment of the USArray Transportable Array (TA) stations (Fig. 1a), have yielded considerable improvements in information about anisotropy in the shallow Earth beneath the western US. Here we measure Rayleigh wave phase travel times based on ambient noise¹⁸ at periods from 12 to 46 s using observations from 611 TA stations that operated between October 2004 and October 2008 (ref. 12). Similar measurements from 24 to 54 s period are obtained from 574 teleseismic earthquakes with $M_s \geq 5.0$ that occurred between January 2006 and January 2009. These surface wave dispersion measurements are used to infer azimuthal anisotropy in the crust and uppermost mantle and, combined with SKS splitting measurements⁹ (Fouch and West, manuscript in preparation), also constrain azimuthal anisotropy in the asthenospheric mantle.

The surface wave tomographic method is Eikonal tomography¹⁷, which estimates azimuthally dependent phase velocity and its uncertainty on a 0.2° spatial grid (Fig. 1b–g). This method produces direct observation of the 180° azimuthal periodicity of Rayleigh wave speeds (Fig. 1b–g) that is expected for a weakly anisotropic medium¹⁹, yielding a fast azimuth direction and amplitude of anisotropy at each period and grid node. The robustness and uncertainty (see Methods) of the observed anisotropy are verified

by comparing the independent results from the ambient noise and earthquake data sets (Supplementary Fig. S1). Measurements from ambient noise and earthquake tomography are averaged in the period band of overlap. Above 54 s period, wavefield complexities such as multipathing and wavefront healing degrade the ability of Eikonal tomography to recover accurate information about azimuthal anisotropy.

Figure 2a–c summarizes observations of Rayleigh wave azimuthal anisotropy at periods of 12, 26 and 38 s, which are most sensitive to V_{SV} anisotropy in the middle crust, lower crust and uppermost mantle, and uppermost mantle, respectively. The most likely cause of anisotropy is the lattice preferred orientation of crustal or mantle minerals^{20,21}. The patterns of anisotropy at 12 and 38 s period are strikingly different, which requires that anisotropy differ between the crust and uppermost mantle. Figure 2d,e exemplifies the period dependence of the fast azimuths and amplitudes of anisotropy, which we refer to as ‘anisotropic dispersion curves’, for a point in northern Nevada (star in Fig. 1a) where the fast directions at short (<18 s) and long (>32 s) periods differ from one another. The anisotropic dispersion curves are used to invert for three models of anisotropy in the crust and upper mantle (models A, B, C) that differ in the treatment of the deepest (asthenospheric) layer (> ~100 km depth) and in the introduction of SKS splitting measurements in the construction of models B and C.

Model A is based exclusively on the surface wave anisotropic dispersion curves and possesses two vertically constant anisotropic layers: in the middle-to-lower crust and in the uppermost mantle (see Methods) to a depth of about 250 km. The data constrain the model only to about 100 km. The isotropic¹³ and anisotropic parts of this model are summarized in Fig. 3a,b. (Supplementary Figs S2 and S3 present χ^2 misfit and model uncertainties.) Azimuthally averaged SKS splitting measurements are computed using the method of ref. 22 and measurements predicted from model A are compared with SKS observations in Supplementary Fig. S4. The agreement between model A, derived from surface wave data alone, and SKS measurements in which the standard deviation of the difference in fast axis directions averages $\sim 29^\circ$ is unprecedented²³, but is not as good as expected based on the uncertainties of the model ($\sim 16^\circ$ for anisotropic amplitudes greater than 0.75%). This motivates further layerization in the upper mantle and the construction of models B and C.

In models B and C, the anisotropy in the crust and uppermost mantle are the same as model A. The thickness of the uppermost mantle layer, however, and the characteristics of the underlying ‘asthenospheric’ layer are determined from the SKS data (see Methods). (The term ‘asthenospheric layer’ is used for simplicity,

¹Center for Imaging the Earth's Interior, Department of Physics, University of Colorado at Boulder, Boulder, Colorado 80309, USA, ²School of Earth and Space Exploration, Arizona State University, Tempe, Arizona 85287, USA. *e-mail: linf@colorado.edu.

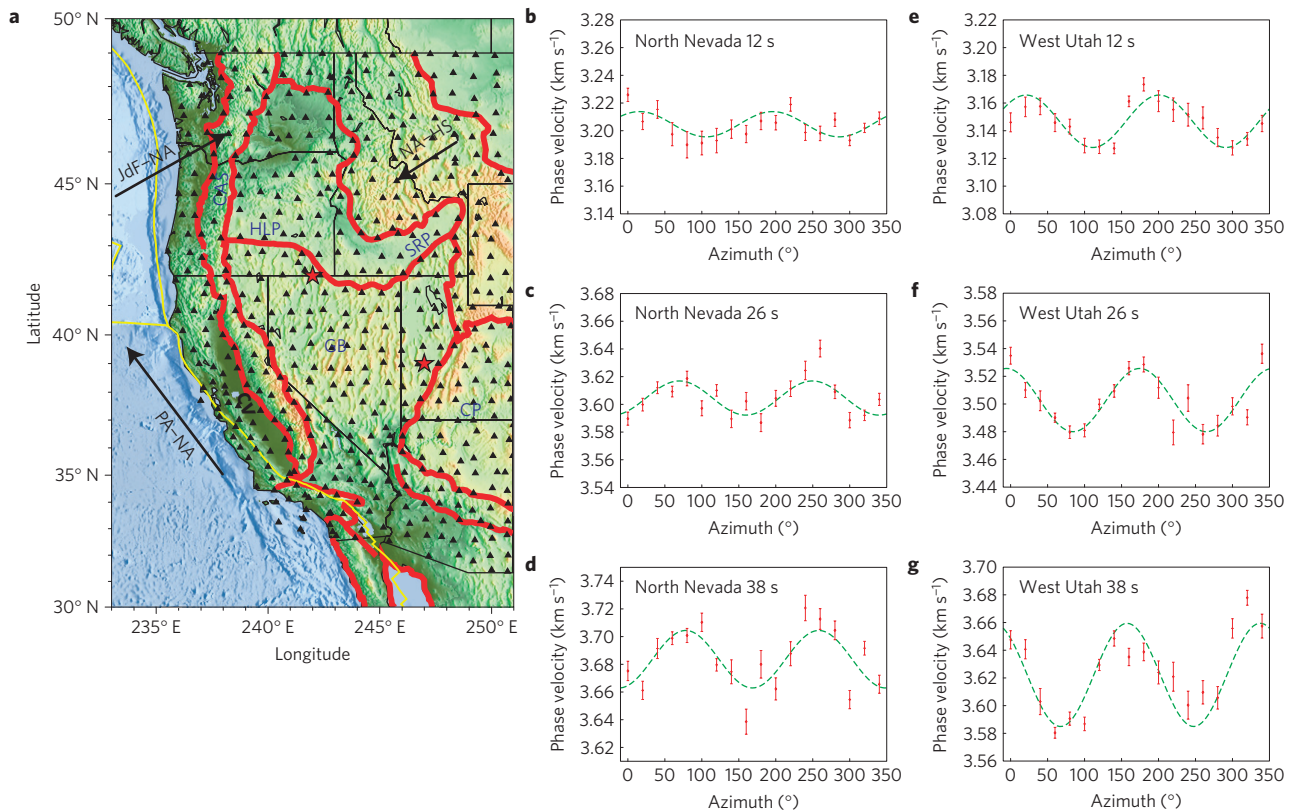


Figure 1 | Major tectonic setting and examples of 2-psi azimuthal anisotropy for Rayleigh waves. **a**, Triangles identify the seismic stations. Yellow and red lines are the plate and tectonic boundaries. CAS: Cascade Range; CV: Central Valley; GB: Great Basin; HLP: High Lava Plains; CP: Colorado Plateau; SRP: Snake River Plain. Black arrows give relative motions between the Pacific (PA) and North American plates (NA), the Juan de Fuca plate (JdF) and NA, and NA and the hotspot reference frame (HS; ref. 24). Red stars give locations shown in **b-g** and Fig. 2d,e. **b-g**, Examples of 12-, 26- and 38-s-period Rayleigh wave phase velocity measurements. Green dashed lines give the best fitting 2-psi curves.

although it is a rheological term and in some regions the layer may be lithospheric and in other regions the overlying uppermost mantle may be asthenospheric.) The fit to the SKS data is optimized when the uppermost mantle layer extends only to a depth of ~ 110 km (80 km beneath the Moho) and the splitting time of the asthenospheric layer is ~ 0.8 s. Although the thickness of the asthenospheric layer is unconstrained by the data, if we assume an anisotropic strength of 2% in this layer, the 0.8 s splitting time requires a thickness of about 200 km beneath the uppermost mantle layer. Asthenospheric anisotropy in models B and C is vertically constant, horizontally constant in model B, but fast axis directions are allowed to vary smoothly laterally in model C (see Methods). Table 1 presents misfit statistics to the surface wave anisotropic dispersion curves and to the SKS data for all three models.

The constant asthenospheric fast direction of model B is 15° N of E. The misfit improvement relative to model A is significant (see Table 1 and Supplementary Fig. S5), although only two asthenospheric parameters (fast axis direction and split time) are introduced across the entire region. This deeper layer of anisotropy, therefore, is probably significantly less laterally heterogeneous than the crust and uppermost mantle.

The fast directions and their uncertainties of the asthenospheric layer in model C are shown in Fig. 3c and Supplementary Fig. S6, respectively. Figure 3d summarizes the predicted SKS apparent splitting parameters from model C. Figure 4a–c compares observed SKS splitting and predictions from model C. The standard deviation of the directional differences equals 18° , consistent with differences expected from model and data uncertainties. About 80% of the model predictions agree with the SKS fast directions by better than 20° , although model C underestimates splitting times

by ~ 0.25 s, on average. Thus, model C successfully reconciles surface wave observations and SKS splitting measurements to within expectations based on data and model uncertainties and resolution.

A strong coherence is observed between the patterns of crustal anisotropy (Fig. 3a) with major geological provinces. This includes crustal north–south fast directions across nearly the entire Great Basin province coincident with strong crustal radial anisotropy¹⁰, northwest–southeast fast directions in California’s Central Valley, east–west fast directions in the Cascadia forearc roughly parallel to the subduction direction of the Juan de Fuca plate, northeast–southwest fast directions in the Colorado Plateau, east–west fast directions in Oregon’s High Lava Plains, and weak anisotropy in the Snake River Plain. It is reasonable to believe that the cause of crustal anisotropy is the same in each geological province.

Spatial patterns of anisotropy in the uppermost mantle (Fig. 3b), on the other hand, are less well correlated with surface geological features, but are correlated with low isotropic velocity anomalies, which probably reflect warm mantle temperatures. For example, strong anisotropy is observed near the western (western Nevada through Oregon’s High Lava Plains) and eastern (western Utah) boundaries of the Great Basin, where isotropic shear wave speeds are low in the uppermost mantle. Not surprisingly, uppermost mantle anisotropy also reflects changes in the ambient stress field. For example, near the western plate boundaries, fast directions change abruptly near the Mendocino Triple Junction, consistent with a change in the principal stress direction from strike-slip in the south to subduction in the north.

The patterns and the overall fast directions of anisotropy in the crust and the uppermost mantle, therefore, are largely uncorrelated

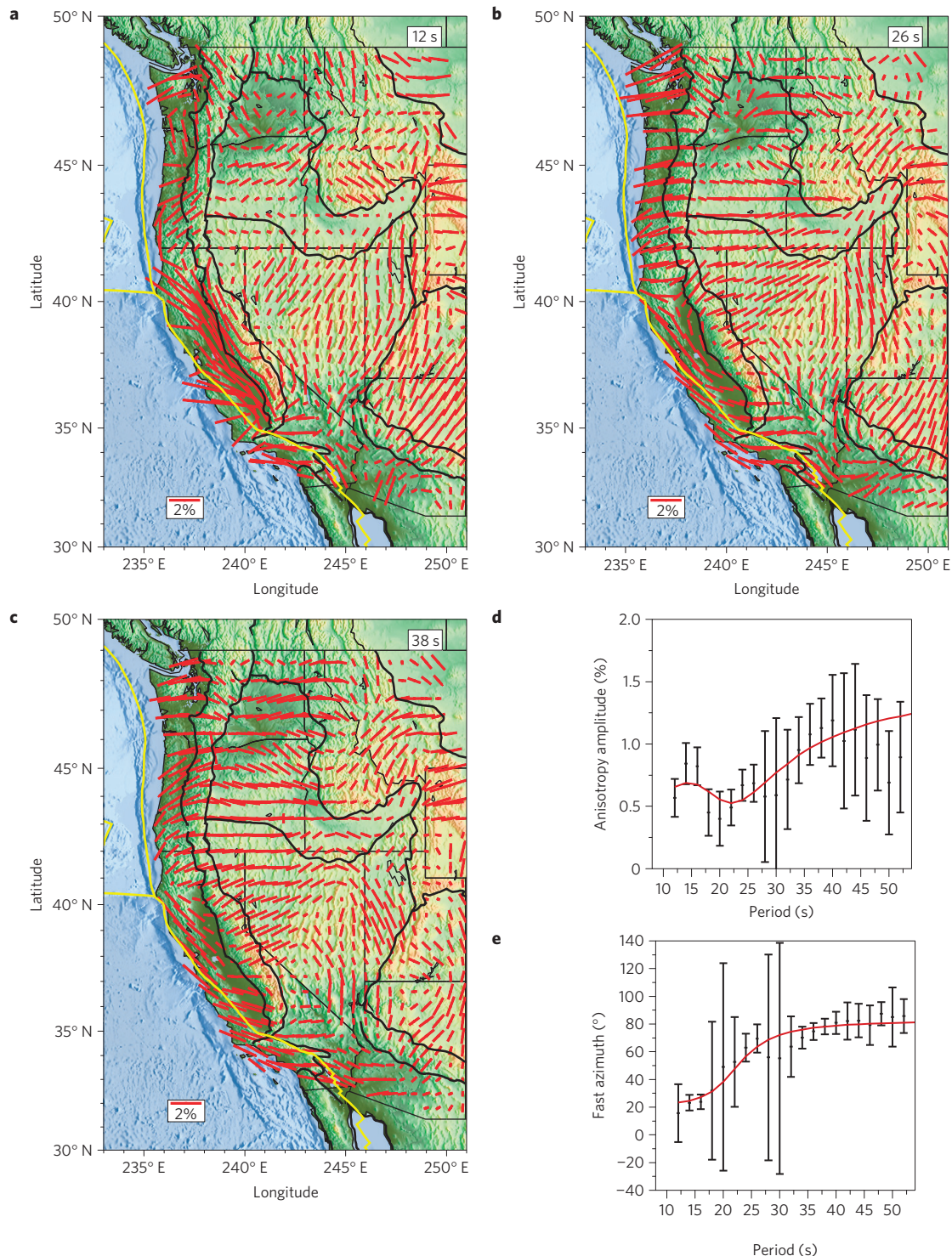


Figure 2 | Example azimuthal anisotropy variation and dispersion in the study region. a–c, Maps of 12, 26 and 38 s period Rayleigh wave phase velocity azimuthal anisotropy on a 0.6° spatial grid. The fast propagation direction and anisotropic amplitude are presented by the orientation and length of the red bars. **d,e,** An example of anisotropy dispersion curves for a location in northern Nevada between periods of 12 and 54 s with associated uncertainties. The red lines are the best fitting dispersion curves based on the crustal and uppermost mantle model shown in Fig. 3a,b.

(Fig. 4d). The directional correlation coefficient between the crustal and uppermost mantle fast axis distributions is found to be $r = 0.12$; one out of four random directional distribution pairs correlate at least as well (see Supplementary Methods). The average strength of uppermost mantle anisotropy across the study area is $\sim 1.3\%$, slightly stronger than the $\sim 1.1\%$ anisotropy observed in the crust.

The smoothly varying anisotropic fast directions in the asthenospheric layer of model C can be approximately separated into three distinct tectonic regions. First, in the east, the fast directions (blue shades in Fig. 3c) average about $32^\circ (\pm 12^\circ)$ north of east, aligned with the direction of absolute plate motion (33° south of west; ref. 24) beneath the North American craton. Second, nearly east–west fast directions are observed beneath most of

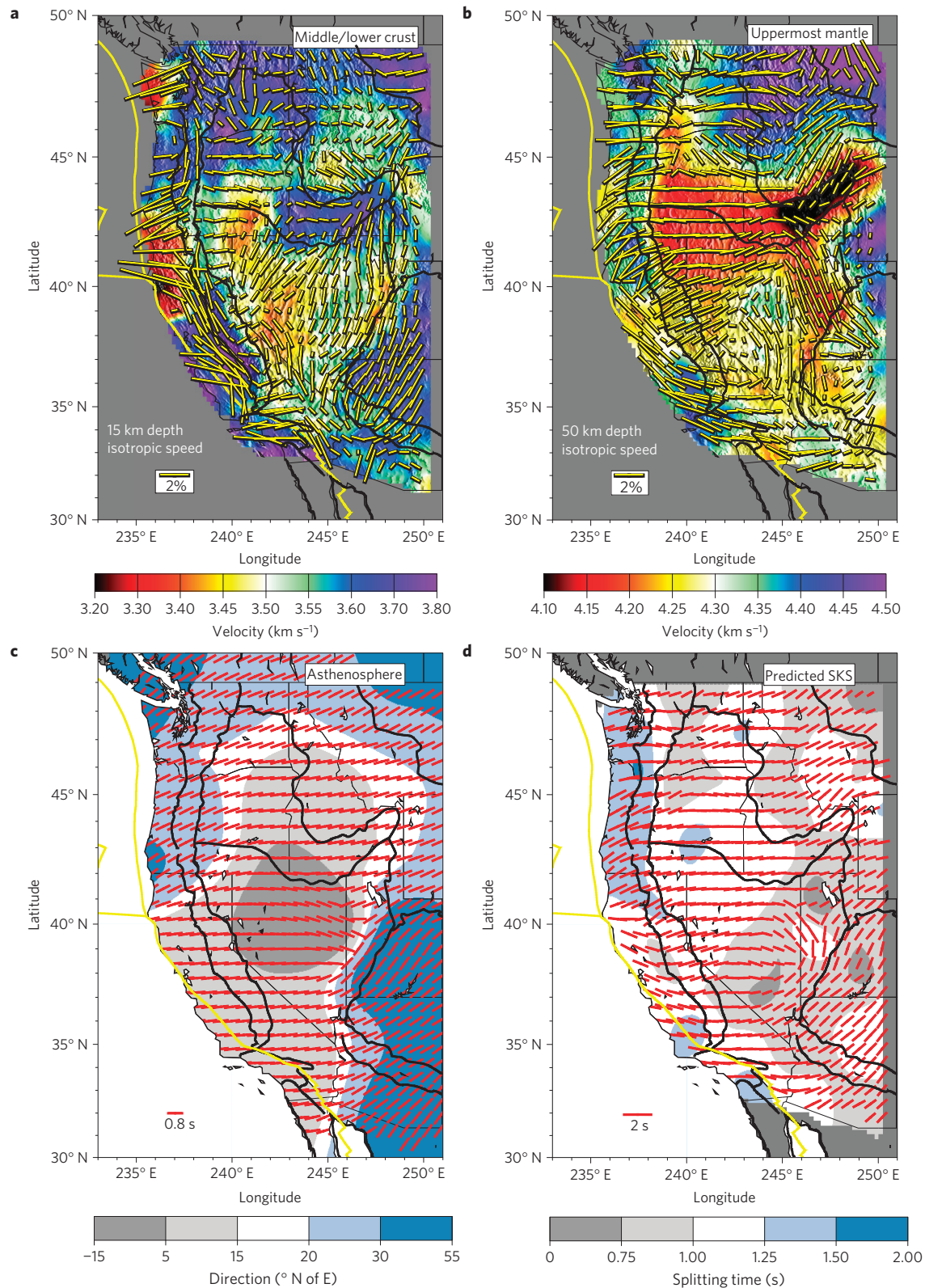


Figure 3 | Azimuthal anisotropy in the crust, uppermost mantle, and asthenosphere and predicted SKS splitting. a, b, Crust and uppermost mantle in models A, B and C. **c,** Asthenospheric layer in model C. Fast propagation directions and anisotropic amplitudes are given by the orientations and lengths of the yellow/red bars on a 0.6° spatial grid. Background colours represent isotropic shear wave speeds at depths of 15 and 50 km in **a, b**, and the fast direction is shown in the background in **c, d**. Predicted SKS measurements based on model C, where the background colour also gives the split time.

the tectonically active western US, which may be induced by a combination of absolute plate motions and the geodynamic effect of the previously subducted Farallon slab^{4,6}, as well as rapid

eastwards inflow of Pacific asthenosphere in the gap between the Mendocino and Rivera triple junctions where subduction has been eradicated. Third, north of the Mendocino Triple Junction

Table 1 | Summary of model performance.

| | Variance reduction relative to an isotropic model | | Comparison between predicted and observed SKS fast directions | |
|---|---|------------------------|---|---------------------------|
| | Surface wave data (%) | SKS splitting data (%) | Standard deviation | Percentage within 20° (%) |
| Model A: Crust and 220-km-thick uppermost mantle. | 94 | 36 | 29° | 57 |
| Model B: Crust, 80-km-thick uppermost mantle, with a laterally homogeneous asthenosphere. | 94 | 58 | 22° | 77 |
| Model C: Crust, 80-km-thick uppermost mantle, with a laterally smoothly varying asthenosphere. | 94 | 64 | 18° | 82 |

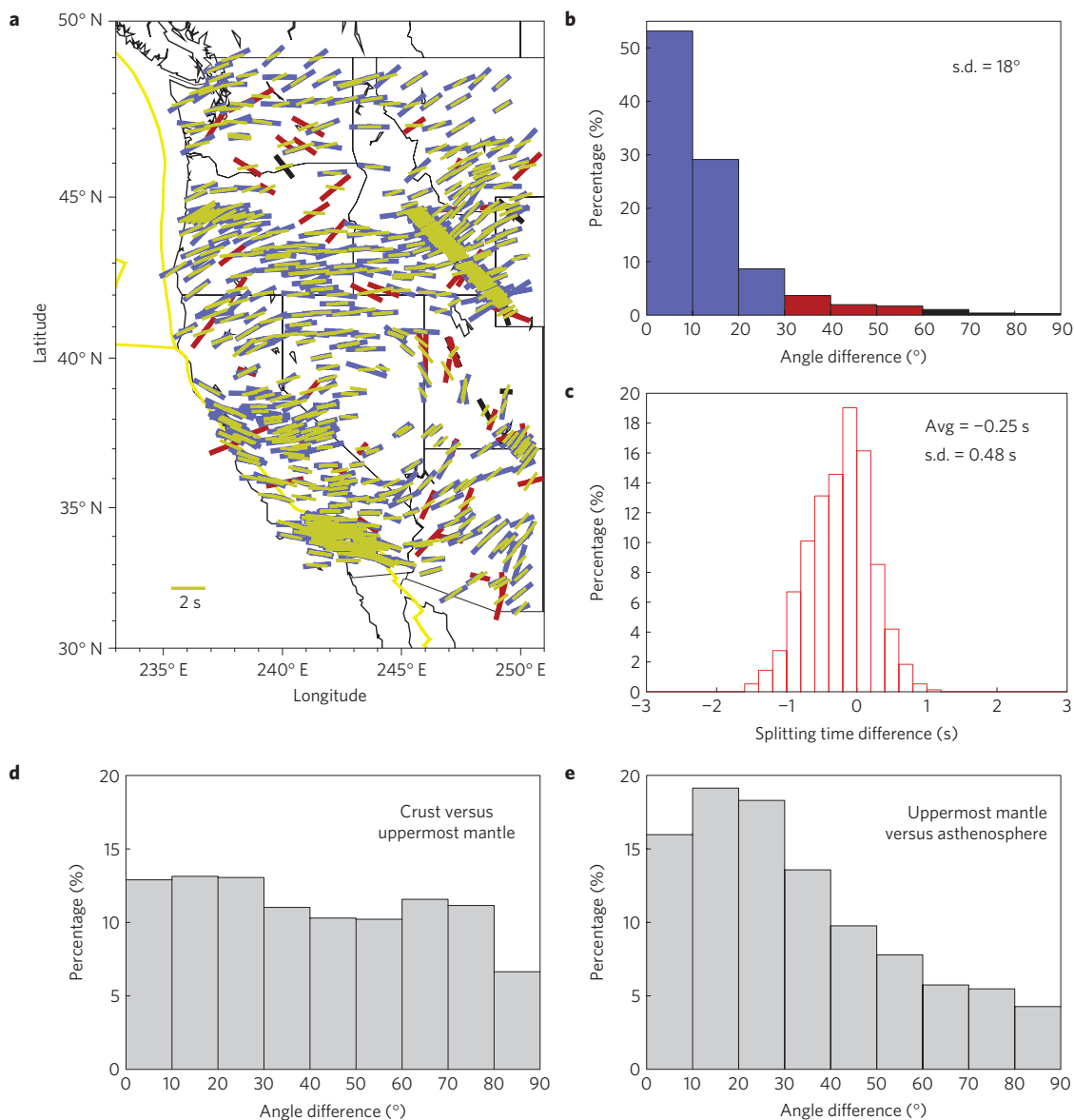


Figure 4 | Comparison of predicted and observed SKS splitting and comparison of anisotropy between different layers. a, Observed SKS splitting (blue, red or black) compared with predictions (yellow) from model C (Fig. 3a–c) where bars summarize the fast direction and splitting time. Blue, red or black colours give differences in fast directions: blue: 0°–30°, red: 30°–60°, black: 60°–90°. **b, c,** Differences between the observed and predicted (model C) directions and times in **a**. **d,** Differences in fast directions between the crust and uppermost mantle. **e,** Differences in fast directions between the uppermost mantle and the asthenosphere in model C.

in Cascadia, there is a distinct region with fast directions nearly parallel to the northeast-directed subduction of the Juan de Fuca plate (Fig. 1a). There is only weak directional agreement between the uppermost mantle and asthenospheric fast directions (Fig. 4e), but agreement is best where shear velocities are slow (that is, hot) and the lithosphere is thinnest. Uppermost mantle anisotropy in cool (that is, fast) regions may be 'frozen-in', whereas anisotropy in warm regions may continue to evolve with the current sub-crustal deformation.

Numerous studies have used shear wave splitting measurements to infer sub-lithospheric flow beneath the western US (refs 3–6, 8,9). The spatial pattern of broad-scale asthenospheric anisotropy in model C reconciles earlier studies that have suggested that sub-lithospheric anisotropy is induced by absolute plate motions⁷ or the subduction of the Juan de Fuca and Farallon slabs^{4,6,8}, as spatially dependent correlations between absolute plate motions and expected subduction induced anisotropy are both observed in model C. In addition, the observation of fast directions parallel to the San Andreas fault in the uppermost mantle is consistent with the deformation direction induced by simple shear²⁵. East–west asthenospheric fast directions in this area, in contrast, suggest that plate interaction deformation does not penetrate to asthenospheric depths similar to previous SKS splitting studies near the San Andreas fault^{2,5}.

The observed disagreement between the strength, geometry and geological coherence of anisotropy in the crust and uppermost mantle across much of the western US presents prima facie evidence against a model of simple mechanical coupling between these layers, which has been suggested for regions of thicker lithosphere²⁶. Our model, therefore, presents new constraints on strain partitioning within the crust and upper mantle and on geodynamical models of deformation within and beneath the lithosphere. It must be acknowledged, however, that application of these constraints, at least in the near term, will be impeded by ignorance of the crustal minerals that cause the anisotropy as well as incomplete knowledge of their anisotropic properties.

Methods

Uncertainty of azimuthal anisotropy based on Eikonal tomography. Ref. 17 discusses the estimation of uncertainty for the two anisotropic dispersion parameters (period dependent fast axis direction and amplitude) shown, for example, in Fig. 2d,e. To prevent underestimation of uncertainties, two additional uncertainty scaling schemes are applied. First, the reduced chi-squared value of the best fitting 2-psi curve (for example, green dashed line in Fig. 1b–g), $\chi_{2\text{-psi}}^2$, is used to scale the uncertainty of both parameters by $\lambda = \exp(\chi_{2\text{-psi}}^2/6)$. The effect is to scale up uncertainties at periods where data misfit is large. Second, if the anisotropy amplitude, c , is less than 0.75% we scale the fast direction uncertainty by $\lambda = 8.5\text{--}10c$, which acts to diminish the effect of fast direction measurements where amplitudes are small in the ensuing inversion. Supplementary Fig. S1e,f demonstrates that this approach yields measurement uncertainties consistent with the differences between ambient noise and earthquake tomography, although perhaps slightly underestimated.

Weakly anisotropic medium. For a weak anisotropic medium, there are 13 independent elastic moduli that determine surface wave observables: the five Love parameters (A, C, F, L and N) that define a transversely isotropic medium (for a transversely isotropic medium: $A = \rho V_{\text{PH}}^2$, $N = \rho V_{\text{SH}}^2$, $L = \rho V_{\text{SV}}^2$, where ρ is density) and six 2-psi ($B_{c,s}$, $G_{c,s}$, and $H_{c,s}$) and two 4-psi ($E_{c,s}$) azimuthal anisotropy parameters^{7,21} (subscripts c and s indicate cosine and sine terms, respectively). In principle, the Love parameters can be determined by a constrained joint inversion of Love and Rayleigh wave isotropic dispersion curves¹⁰. The remaining eight azimuthal anisotropy parameters are required to explain the directionally dependent phase velocity measurements.

Inversion of anisotropic dispersion curves. We invert the anisotropic dispersion curves at each location for a 3D azimuthally anisotropic shear velocity model of the crust and uppermost mantle. First, we follow the method of ref. 10 to construct a reference isotropic model represented by four crustal layers and five B-splines in the upper mantle. Second, we introduce azimuthal anisotropy perturbations to the isotropic model to fit the anisotropic dispersion curves observed at each location. Most observed anisotropic dispersion curves fit well to a two-layer anisotropic

model (Fig. 2d,e; Supplementary Fig. S2) in which azimuthal anisotropy is introduced in the middle-to-lower crust and in the uppermost mantle. Anisotropy in each layer is vertically constant but laterally variable.

Only the anisotropic shear moduli $G_{c,s}$ are explicitly estimated in the inversion. The moduli $H_{c,s}$ and $E_{c,s}$ are not included because their effects on Rayleigh wave phase velocities are negligible based on empirical mineral models²¹ and the non-existence of 4-psi anisotropy in our directionally dependent phase velocity measurements (for example, Fig. 1b–g). The sensitivities of Rayleigh wave anisotropic dispersion measurements to $G_{c,s}$ and the compressional moduli $B_{c,s}$ are identical to the sensitivities of isotropic Rayleigh wave dispersion curves to the Love parameters L and A (ref. 21), respectively. The ratios $G_{c,s}/L$ and $B_{c,s}/A$ are associated with azimuthal variations of horizontally propagating body wave speeds V_{SV} and V_{PH} , respectively. Although our surface wave anisotropy measurements are roughly three times more sensitive to $G_{c,s}/L$ than $B_{c,s}/A$ (Supplementary Fig. S7), there is a formal tradeoff between the two that prevents estimating them independently. Therefore, in estimating $G_{c,s}$, we impose the relationship $B_{c,s}/A = G_{c,s}/L$. This is based on studies of olivine²¹ as well as mica- and amphibole-rich crustal rocks²⁰ that indicate that $G_{c,s}$ and $B_{c,s}$ may have similar fast and slow directions and that the ratios $B_{c,s}/A$ and $G_{c,s}/L$ are also similar. This approach is identical to fixing the ratio $V_{\text{PH}}/V_{\text{SV}}$ for body waves propagating in different azimuthal directions. This choice has no effect on the inferred anisotropic fast directions, but reasonable variations in the scaling between $G_{c,s}/L$ and $B_{c,s}/A$ would affect the amplitude of anisotropy.

Uppermost mantle thickness and asthenospheric anisotropy parameters. To determine model B, we minimized the SKS misfit (defined in Supplementary Methods) with three free parameters: uppermost mantle thickness, asthenospheric splitting strength, and asthenospheric fast direction, which are constant across the entire region. The crustal and uppermost mantle anisotropic parameters constrained by surface wave data are fixed in the inversion. The misfit is minimized for an 80-km-thick uppermost mantle and an asthenospheric layer with 0.8 s splitting strength and 15° north of east fast direction.

To ensure only smooth lateral variations of asthenospheric fast directions in model C, we first fix the uppermost mantle thickness and asthenospheric splitting strength based on model B. For each location we then minimize the misfit between the predicted and observed SKS measurements within a radius of 300 km by assuming a constant fast direction in the asthenospheric layer. The tradeoff between splitting strength in the asthenospheric layer and the thickness of the uppermost mantle layer increases the difficulty of investigating the spatial variation of these two parameters. This smoothing process effectively weights down the effect of small-scale variations in the SKS measurements.

Received 15 April 2010; accepted 12 November 2010;
published online 12 December 2010

References

1. Savage, M. K. Seismic anisotropy and mantle deformation: What have we learned from shear wave splitting? *Rev. Geophys.* **37**, 65–106 (1999).
2. Ozalaybey, S. & Savage, M. K. Shear-wave splitting beneath western United States in relation to plate tectonics. *J. Geophys. Res.* **100**, 18135–18149 (1995).
3. Savage, M. K. & Sheehan, A. F. Seismic anisotropy and mantle flow from the Great Basin to the Great Plains, western United States. *J. Geophys. Res.* **105**, 13715–13734 (2000).
4. Silver, P. & Holt, W. The mantle flow field beneath western North America. *Science* **295**, 1054–1057 (2002).
5. Savage, M. K. Seismic anisotropy and mantle deformation in the western United States and southwestern Canada. *Int. Geol. Rev.* **44**, 913–937 (2002).
6. Becker, T. W., Schulte-Pelkum, V., Blackman, D. K., Kellogg, J. B. & O'Connell, R. J. Mantle flow under the western United States from shear wave splitting. *Earth Planet. Sci. Lett.* **247**, 235–251 (2006).
7. Marone, F. & Romanowicz, B. The depth distribution of azimuthal anisotropy in the continental upper mantle. *Nature* **447**, 198–201 (2007).
8. Zandt, G. & Humphreys, E. Toroidal mantle flow through the western US slab window. *Geology* **36**, 295–298 (2008).
9. West, J. D., Fouch, M. J., Roth, J. B. & Elkins-Tanton, L. T. Vertical mantle flow associated with a lithospheric drip beneath the Great Basin. *Nature Geosci.* **2**, 438–443 (2009).
10. Moschetti, M. P., Ritzwoller, M. H., Lin, F. & Yang, Y. Seismic evidence for widespread western-US deep-crustal deformation caused by extension. *Nature* **464**, 885–889 (2010).
11. Buehler, J. S. & Shearer, P. M. Pn tomography of the western United States using USArray. *J. Geophys. Res.* **115**, B09315 (2010).
12. Lin, F., Moschetti, M. P. & Ritzwoller, M. H. Surface wave tomography of the western United States from ambient seismic noise: Rayleigh and Love wave phase velocity maps. *Geophys. J. Int.* **173**, 281–298 (2008).
13. Yang, Y., Ritzwoller, M. H., Lin, F., Moschetti, M. P. & Shapiro, N. M. Structure of the crust and uppermost mantle beneath the western United States revealed by ambient noise and earthquake tomography. *J. Geophys. Res.* **113**, B12310 (2008).

14. Sabra, K. G., Gerstoft, P., Roux, P., Kuperman, W. A. & Fehler, M. C. Surface wave tomography from microseisms in Southern California. *Geophys. Res. Lett.* **32**, L14311 (2005).
15. Shapiro, N. M., Campillo, M., Stehly, L. & Ritzwoller, M. H. High-resolution surface-wave tomography from ambient seismic noise. *Science* **307**, 1615–1618 (2005).
16. Pollitz, F. F. Observations and interpretation of fundamental mode Rayleigh wavefields recorded by the Transportable Array (USArray). *J. Geophys. Res.* **113**, B10311 (2008).
17. Lin, F., Ritzwoller, M. H. & Snieder, R. Eikonal tomography: Surface wave tomography by phase front tracking across a regional broad-band seismic array. *Geophys. J. Int.* **177**, 1091–1110 (2009).
18. Bensen, G. D. *et al.* Processing seismic ambient noise data to obtain reliable broad-band surface wave dispersion measurements. *Geophys. J. Int.* **169**, 1239–1260 (2007).
19. Smith, M. L. & Dahlen, F. A. Azimuthal dependence of Love and Rayleigh-wave propagation in a slightly anisotropic medium. *J. Geophys. Res.* **78**, 3321–3333 (1973).
20. Barruol, G. & Kern, H. Seismic anisotropy and shear-wave splitting in lower-crustal and upper-mantle rocks from the Ivrea zone—experimental and calculated data. *Phys. Earth Planet. Inter.* **95**, 175–194 (1996).
21. Montagner, J.-P. & Nataf, H.-C. A simple method for inverting the azimuthal anisotropy of surface waves. *J. Geophys. Res.* **91**, 511–520 (1986).
22. Rumpker, G. & Silver, P. G. Apparent shear-wave splitting parameters in the presence of vertically varying anisotropy. *Geophys. J. Int.* **135**, 790–800 (1998).
23. Montagner, J.-P., Griot-Pommera, D.-A. & Lavé, J. How to relate body wave and surface wave anisotropy? *J. Geophys. Res.* **105**, 19015–19027 (2000).
24. Gripp, A. E. & Gordon, R. G. Young tracks of hotspots and current plate velocities. *Geophys. J. Int.* **150**, 321–361 (2002).
25. Zhang, S. Q. & Karato, S. Lattice preferred orientation of olivine aggregates deformed in simple shear. *Nature* **375**, 774–777 (1995).
26. Holt, W. E. Correlated crust and mantle strain fields in Tibet. *Geology* **28**, 67–70 (2000).

Acknowledgements

Instruments [data] used in this study were made available through EarthScope (<http://www.earthscope.org>; EAR-0323309), supported by the National Science Foundation. The facilities of the IRIS Data Management System, and specifically the IRIS Data Management Center, were used for access to waveform and metadata required in this study. The IRIS DMS is funded through the National Science Foundation and specifically the GEO Directorate through the Instrumentation and Facilities Program of the National Science Foundation under Cooperative Agreement EAR-0552316. This work has been supported by NSF grants EAR-0711526 and EAR-0844097.

Author contributions

F.-C.L. carried out ambient noise and earthquake tomography for the Rayleigh-wave measurements, computed the three-dimensional inversion and co-wrote the paper. M.H.R. guided the study and co-wrote the paper. Y.Y. and M.P.M. contributed surface-wave analysis tools. M.J.F. assembled and carried out SKS splitting measurements. All authors discussed the results and provided comments on the manuscript.

Additional information

The authors declare no competing financial interests. Supplementary information accompanies this paper on www.nature.com/naturegeoscience. Reprints and permissions information is available online at <http://npg.nature.com/reprintsandpermissions>. Correspondence and requests for materials should be addressed to F.-C.L.